Quantitative Raman spectroscopy in turbid media

Carina Reble
Technical University Berlin
Institute for Optics and Atomic Physics
10587 Berlin, Germany
and
Laser- und Medizin-Technologie Berlin (LMTB)
Fabeckstraße 60-62
14195 Berlin, Germany

Ingo Gersonde
Laser- und Medizin-Technologie Berlin (LMTB)
Fabeckstraße 60-62
14195 Berlin, Germany

Stefan Andree
Hans Joachim Eichler
Technical University Berlin
Institute for Optics and Atomic Physics
10587 Berlin, Germany
and
Laser- und Medizin-Technologie Berlin (LMTB)
Fabeckstraße 60-62
14195 Berlin, Germany

Jürgen Helfmann
Laser- und Medizin-Technologie Berlin (LMTB)
Fabeckstraße 60-62
14195 Berlin, Germany

Abstract. Intrinsic Raman spectra of biological tissue are distorted by the influences of tissue absorption and scattering, which significantly challenge signal quantification. A combined Raman and spatially resolved reflectance setup is introduced to measure the absorption coefficient μ_a and the reduced scattering coefficient μ_s' of the tissue, together with the Raman signals. The influence of μ_a and μ_s' on the resonance Raman signal of β-carotene is measured at 1524 cm^{-1} by tissue phantom measurements and Monte Carlo simulations for μ_a=0.01 to 10 mm^{-1} and μ_s'=0.1 to 10 mm^{-1}. Both methods show that the Raman signal drops roughly proportional to $1/\mu_a$ for $\mu_a > 0.2$ mm^{-1} in the measurement geometry and that the influence of μ_s' is weaker, but not negligible. Possible correction functions dependent on the elastic diffuse reflectance are investigated to correct the Raman signal for the influence of μ_a and μ_s', provided that μ_a and μ_s' are measured as well. A correction function based on the Monte Carlo simulation of Raman signals is suggested as an alternative. Both approaches strongly reduce the turbidity-induced variation of the Raman signals and allow absolute Raman scattering coefficients to be determined.
[DOI: 10.1117/1.3456370]

Keywords: Raman spectroscopy; intrinsic Raman spectroscopy; quantitative Raman spectroscopy; spatially resolved reflectance; tissue diagnostics; lookup table.

Paper 09419PR received Sep. 28, 2009; revised manuscript received Apr. 6, 2010; accepted for publication May 5, 2010; published online Jun. 30, 2010.

1 Introduction

Raman spectroscopy is a powerful analytical method due to its chemical bond specificity. The molecular vibrations of each substance produce a characteristic fingerprint spectrum that can be used to determine the chemical and structural composition of the sample. Applications in biomedical research are wide-ranging, including the diagnosis of cancer,[1–3] atherosclerosis,[4] and blood analysis.[5] The major advantages of Raman spectroscopy compared to fluorescence applications are that Raman signals do not bleach, and that Raman bands are spectrally narrow, which improves the separability of the signals.

A basic challenge for Raman spectroscopic measurements in turbid media is the signal quantification. The spectral line shape and overall intensity of the measured spectra depend on the absorption and scattering properties of the sample. In the case of biological tissue, absorption arises from chromophores such as hemoglobin and melanin. Light scattering in tissue occurs due to the refractive index inhomogeneities of the cell nuclei, cell organelles, or collagen fibers. Due to different biochemical tissue compositions and microstructures, the optical properties of tissues may vary strongly between tissues, tissue sites, and individuals. Since a contrast in optical properties can, on its own, indicate pathological changes such as tumor angiogenesis or dysplasia, extensive research has been carried out on the measurement of optical properties for diagnostic purposes.[6–9] Nevertheless, most Raman spectroscopic tissue measurements are not corrected for these influences, which hinders the quantitative comparison of the measured Raman spectra.

Since the measured Raman scattered light and purely elastically scattered light are both influenced by variations in the optical properties, correction methods have been suggested based on diffuse reflectance measurements. Some approaches have been developed for applications where either absorption or scattering is assumed to change[10,11] and are therefore not suitable for *in vivo* applications, where independent and simultaneous variations of the optical properties are common. The first theoretical and experimental studies on the correction of Raman signals in biological tissue were published recently[12–14] for a parameter range of absorption coefficient μ_a and scattering coefficient μ_s, which are typical for measurements in the near infrared wavelength range (NIR). The correction functions utilize the elastic diffuse reflectance, which is measured in the same excitation-detection geometry as the Raman spectrum. However, knowledge of the total attenuation coefficient given by $\mu_t = \mu_a + \mu_s$ is required,[12,13] or the reduced scattering coefficient μ_s' is used.[14] However, the determination of optical properties from a single elastic reflectance signal requires an elastic diffuse reflectance spec-

Address all correspondence to: Carina Reble, LMTB, Fabeckstraße 60-62, 14195 Berlin. Tel: 00493084492334; Fax 004984492399; E-mail: c.reble@lmtb.de

1083-3668/2010/15(3)/037016/8/$25.00 © 2010 SPIE

trum, together with sample specific assumptions regarding the wavelength dependency of the absorption and scattering coefficients,[15] which reduces the method's flexibility.

The aim of our investigation was to develop a method that could correct Raman signals for the influence of the optical properties in a large parameter range without *a priori* assumptions of the absorption and scattering properties. Therefore, we combined Raman spectroscopy with spatially resolved reflectance measurements.[16] By performing measurements on various homogenous tissue phantoms as well as Monte Carlo simulations, we investigated how the Raman signal depends on the optical properties. To include parameters typical for measurements in the NIR as well as in the visible wavelength range (VIS), μ_a was varied from 0.01 to 10 mm^{-1} and μ_s' from 0.1 to 10 mm^{-1}. These investigations exceed the parameter range of previous studies.[12–14] To correct the Raman signals for the influence of the optical properties, we investigated possible correction functions that are dependent on the elastic diffuse reflectance. We also implemented a correction function based directly on the Monte Carlo simulation of the Raman signals.

2 Experimental Setup and Monte Carlo Simulation

In this section, we explain the Monte Carlo code that was used to simulate the Raman signal and describe our combined Raman and spatially resolved reflectance setup as well as the production of the tissue phantoms.

2.1 *Monte Carlo Model for the Simulation of Raman and Reflectance Signals*

In accordance with our experiments, we assumed that the absorption coefficient μ_a and the coefficient for Raman scattering μ_{Raman} were constant throughout the sample. Because μ_{Raman} was very small, multiple Raman scattering was neglected and the Raman signal was assumed to be proportional to μ_{Raman}. We further assumed a Henyey-Greenstein phase function[12] and an anisotropy factor $g=0.8$ for the elastic scattering processes.

We defined a flux density Φ_{ex} of photons that were not Raman scattered and a flux density Φ_{Raman} of Raman-scattered photons. Since multiple Raman scattering was neglected, both densities could be calculated with the conventional Monte Carlo method described in Ref. 17, which takes into account elastic scattering and absorption. Only the source term was different for both flux densities. For Φ_{ex}, the source term was a boundary condition at the sample surface that corresponded to the excitation light entering the sample. For Φ_{Raman}, the source term was the number density of Raman scattering events given by $n_{Raman}=\Phi_{ex}\times\mu_{Raman}$, which was proportional to the number density of the absorbed excitation photons $n_{abs}=\Phi_{ex}\mu_a=(\mu_a/\mu_{Raman})\times n_{Raman}$. Therefore, n_{abs} was used as the source density to calculate Φ_{Raman} and scale the results with μ_{Raman}/μ_a. In the Monte Carlo calculation for Φ_{ex}, the density n_{abs} was given by the ensemble of absorption process positions. Thus, the following scheme was used to calculate Φ_{Raman}: At each position where an excitation photon was absorbed, a Raman scattered photon was launched with an isotropic initial direction. The photon propagated with optical parameters that corresponded to the Stokes shifted wavelength. A fraction N_{Raman} of these photons was remitted at the sample surface and reached a Raman detector, which was defined as a circular area on the sample surface. Normalization with the number of incident excitation photons N_{ex} and scaling led to the detected Raman signal $Ram_T=(N_{Raman}/N_{ex})\times(\mu_{Raman}/\mu_a)$. In this paper, Ram_T corresponds to the calculated or measured relative Raman signal of a Raman scatterer embedded in a turbid matrix. The elastic diffuse reflectance of the sample was determined by the number of excitation photons $N_{elastic}$ detected at the sample surface. In the results shown below, the relative elastic diffuse reflectance signal is given by $N_{elastic}/N_{ex}$.

The size and position of the excitation and detector area corresponds to the images of the fiber endfaces on the sample surface in Fig. 1. For simplicity, the fiber bundle for the Raman detection in Fig. 2 was assumed to correspond to one fiber with a 0.7-mm radius, and the slant of excitation and receiving optics were neglected. The propagation direction of the remitted photons were analyzed by taking into account the finite numerical aperture (NA) of the imaging optics. For our application, we used NA=1 and scaled the results by a con-

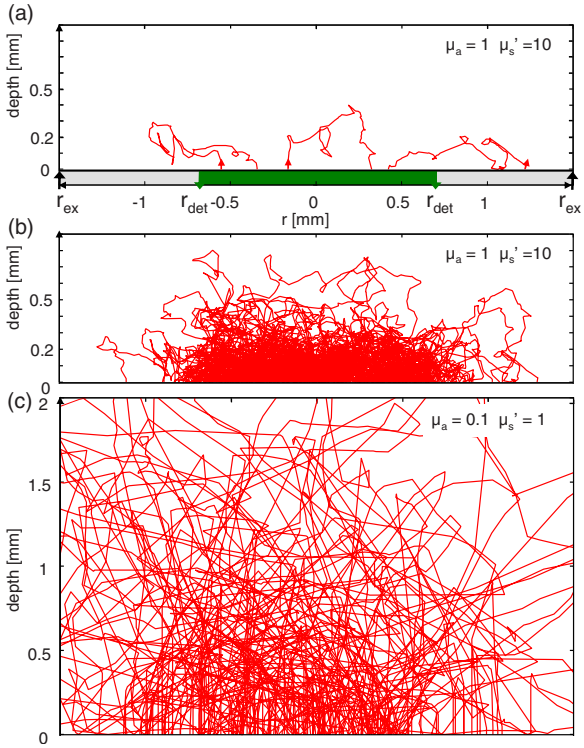

Fig. 1 Monte Carlo simulation for Raman measurements in turbid media illustrated by photon trajectories. Only the trajectories of Raman photons that reached the detector in our measurement geometry (excitation spot with radius $r_{ex}=1.5$ mm and detection spot with radius $r_{det}=0.7$ mm) are plotted. An isotropic Raman scattering event occurred somewhere on each of the shown trajectories. (a) Schematic for three detected Raman photons. (b) Simulation for $\mu_a=1$ mm^{-1} and $\mu_s'=10$ mm^{-1}. (c) Simulation for $\mu_a=0.1$ mm^{-1} and $\mu_s'=1$ mm^{-1}. For simplicity, μ_a and μ_s' correspond to the mean of the optical properties at the Raman and Stokes wavelength. The trajectories in (b) and (c) correspond to 10^3 incident photons, in contrast to the 10^5 to 10^6 photons used to calculate our data.

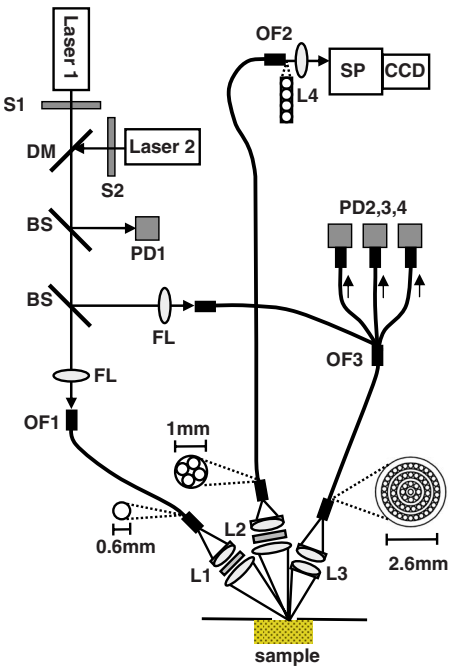

Fig. 2 Experimental setup. S1 and S2: shutters; DM: dichroic mirror; BS: cover slide as beamsplitter; FL: focusing lens; PD1: photodiode for laser reference; PD2 through 4: photodiodes for each ring of reflectance detection fibers of OF3; OF1: optical fiber for Raman excitation; OF2: fiber bundle for Raman detection; and OF3: fiber bundle for spatially resolved reflectance excitation and detection. The central illumination fiber is surrounded by concentric rings of detection fibers at distances r=0.4, 0.8, and 1.3 mm from the center. L1: lens system with magnification M=5, including laser cleanup filter; L2: lens system with M=1.5, including long-pass filter; L3: lens system with M=1; L4: lens system with M=1.8 for coupling to spectrometer (SP).

stant factor accordingly. We used 10^5 photons for $\mu_a > 0.1$ mm^{-1}, leading to a computation time of a few seconds for each set of parameters but 10^6 photons for $\mu_a < 0.1$ mm^{-1}.

2.2 *Combined Raman and Spatially Resolved Reflectance Setup*

A schematic overview of our setup is shown in Fig. 2. For the alternating measurement of Raman spectra and spatially resolved reflectance, we combined a Raman excitation channel, a Raman detection channel, and one channel for the spatially resolved reflectance measurement. The three channels were imaged onto the sample with the optics described in Fig. 2. The laser power for Raman and spatially resolved reflectance measurements was $P \leqslant 2$ mW/mm^2.

2.2.1 *Raman spectroscopy*

The resonance Raman scattering of carotenoids was excited at 488 nm using an argon laser with a cleanup filter (max line, AHF Analysentechnik). For the detection, we used a CCD-based spectrometer (Triax 320, Jobin Yvon) with the CCD chip cooled to −20 °C. We used a 1200-l/mm grating and an exposure time of 10 s for each spectrum. For the following analysis, we evaluated the Raman peak (1524 cm^{-1}) at 527 nm, which originates from the C=C stretch vibrations of β-carotene. In addition, we evaluated the fraction of the elastically scattered laser light at 488 nm, which passed the long pass filter (edge basic, AHF Analysentechnik). To obtain the Raman peak values from the fluorescence background, we performed a nonlinear least square fit of a Lorentzian-shaped curve to the spectra (gnuplot).

2.2.2 *Spatially resolved reflectance measurement*

The spatially resolved reflectance measurement was based on a customized fiber bundle, which consisted of 58 multimode silica fibers, each 200 μm in diameter with NA=0.22 (see Fig. 2, Fiberguide). One central illumination fiber was surrounded by three concentric rings of detection fibers (n=8, 19, and 30). The fiber bundle was imaged onto the sample surface at an angle of 20 deg to avoid detection of specular reflection and to permit the arrangement of the three channels in one plane. The resulting source-detector distances were 0.4, 0.8, and 1.3 mm, which were the average distances of the slightly distorted image. The fibers of each detection ring were bundled and fixed in close proximity to photodiodes (PDB-C160SM, Laser Components). The amplification was varied automatically for each readout to optimize analog-to-digital (A/D) conversion. The background signal was acquired automatically before each measurement and subtracted. The reflectance signals were normalized to the illumination power, which was measured simultaneously (see Fig. 2). The optical properties of the sample were measured at the Raman excitation wavelength with the argon laser at 488 nm and close to the Raman peak with a frequency-doubled Nd:YAG laser at 532 nm. Using lasers instead of white light was motivated by the fact that simple photodiodes could be used for the measurement without spectral filtering of the reflected light.

2.2.3 *Lookup table-based determination of μ_a and μ_s' from spatially resolved reflectance*

In order to infer the optical properties of the samples, we used a lookup table (LUT),[18] which is a table with forward simulations of the reflectance for various combinations of μ_a and μ_s', for each of the source-detector distances given in Fig. 2. The data were produced with the Monte Carlo code described in Sec. 2.1 for the purely elastically scattered photons using a 200-μm detector at the source-detector distances given above. The sample geometry, anisotropy factor, and refractive index (n_r=1.42) were constant within the LUT. The calibration factors for the measured reflectance values, which accounted for the transmission properties of the optics, differences in alignment, and the detector response, were obtained by measuring a set of three calibration phantoms with known optical properties. The measured reflectance values were then compared to the LUT by a customized program.[19] The program output was μ_a and μ_s' of the best-fitting LUT-data.

When the method was evaluated for 15 phantoms with μ_a=0.15 to 0.7 mm^{-1} and μ_s'=1.5 to 6 mm^{-1}, the optical properties differed ⩽20% from the values obtained by integrating sphere measurements (Sec. 2.3).The average deviation was +3% (μ_a) and −5% (μ_s'), and the average absolute deviation was 11% (μ_a) and 10% (μ_s'). This range of optical properties corresponds to the results of preliminary *in vivo* measurements of skin. Since the setup was designed for *in vivo* skin measurements, the illumination power was limited to 2 mW/mm^{-2}. Phantoms with a μ_a higher than 0.7 mm^{-1}

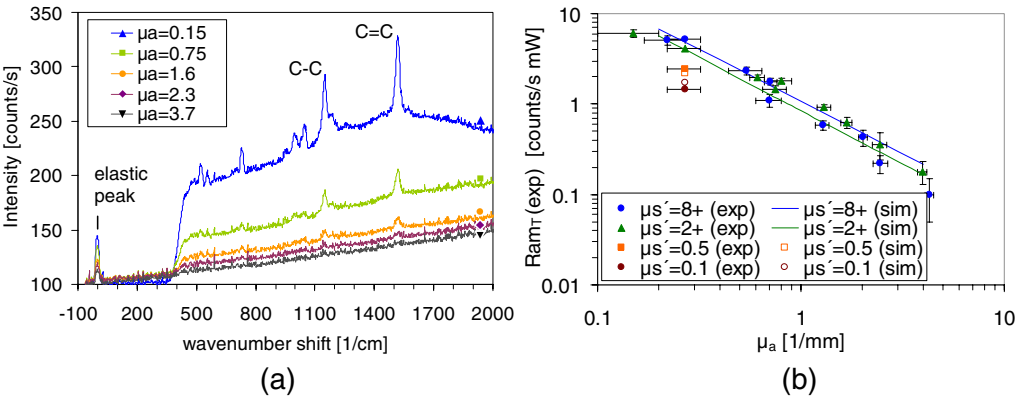

Fig. 3 (a) Raw spectra of silicone phantoms containing the same concentration of β-carotene but with different μ_a of the silicone matrix ($\mu_s'=2+\mathrm{mm}^{-1}$, where "+" indicates that μ_s' was not constant within one series but increased slightly with the absorber concentration). The baselines are aligned, and μ_a and μ_s' correspond to the mean of the optical properties at the Raman and Stokes wavelength in units of 1/mm. (b) Comparison of experimental Ram_T (C═C bonds at 1524 cm^{-1}, filled symbols) and calculated Ram_T (lines or open symbols, fitted to experimental values) dependent on μ_a for various series of μ_s'. The Raman signal error bars represent the standard deviation (SD) of five Raman measurements at different positions. The optical parameter error bars correspond to the uncertainty of the optical property measurements with the integrating sphere.

could not be measured with the current implementation of our setup because there was no reflectance signal detectable at the second distance ($r=0.8$ mm) using 488 nm.

2.3 *Phantom Preparation and Characterization*

Tissue phantoms with $\mu_a=0.2$ to 4 mm^{-1} and $\mu_s'=0.1$ to 8 mm^{-1} were produced based on silicone (Wacker, RT 601) using red silopren color paste (GE Bayer Silicones) as an absorber and titanium dioxide as a scatterer. To ensure that the highly lipophilic β-carotene (Fluka) was completely dissolved, it was first dissolved in methylene chloride and paraffin (Vaseline, Unilever) and then mixed with the silicone. The final β-carotene concentration was 10 μg/ml in all phantoms. The contribution of 10 μg/ml β-carotene to the μ_a of the silicone phantom was 0.07 mm^{-1} at 488 nm, as measured in a transparent phantom. The Raman spectra were measured on the day of preparation. A thin layer from each phantom mixture was used to determine the optical properties with an integrating sphere spectrometer (Lambda 900, Perkin Elmer). The total transmission, diffuse transmission, and diffuse reflectance were measured and used as the input parameters for an inverse Monte Carlo algorithm[20] to yield μ_a, μ_s, and g. For comparison with the spatially resolved reflectance measurements, μ_s' was calculated from μ_s and g.

3 Dependency of the Raman Signal on the Macroscopic Optical Properties

First we investigated how the Raman peak at 1524 cm^{-1} [C═C bonds, see Fig. 3(a)] depends on the optical properties of the silicone phantom, which correspond to typical values for skin in the VIS.[7] The Raman signal dropped roughly proportional to $1/\mu_a$, while the influence of μ_s' was fairly small, see Fig. 3(b). The optical properties of the phantoms are the mean optical coefficients at excitation and Stokes wavelength. These coefficients were measured with the integrating sphere spectrometer, since the whole parameter range was not accessible using our implementation of the spatially resolved reflectance setup. Since the silicone color paste contributed to the scattering coefficient of the phantom, μ_s' of the phantoms was not constant within one series of increasing absorber concentration.

Next we compared our phantom measurements with simulations [Fig. 3(b)]. The simulation results of the Raman signal were all scaled with the same factor to fit the experimental results. The factor includes the unknown *in vivo* Raman cross section as well as setup-specific constants. The trends of the experimental values corresponded well to the simulations. However, the experimental and simulated values did not match for all phantoms within the given errors, which could be explained by errors incurred by variations in the sample preparation.

We further performed Monte Carlo simulations to investigate the dependency of the Raman signal on μ_a and μ_s' in a larger parameter range, as with the phantom measurements (Fig. 4). For our measurement geometry, Ram_T was roughly proportional to $1/\mu_a$ in the VIS ($\mu_a>0.1\mathrm{mm}^{-1}$ and $\mu_s'>1\mathrm{mm}^{-1}$). For smaller μ_a (typical for the NIR), the curves deviated significantly from this behavior. When the same simulation was performed for a pencil-beam excitation and a semi-infinite detection geometry, which is a typical imaging geometry, the $1/\mu_a$ behavior continued into the NIR parameter range (data not shown). When the excitation and detection geometry corresponded to a 200-μm fiber, the μ_a dependency was weaker, as for the measurement geometry used here (data not shown). This can be explained by the influence of the measurement geometry on the pathlength distribution of the detected Raman photons, which determines the influence of the optical properties on the Raman scattered light. For our measurement geometry, the influence of μ_s' in the NIR is larger than the VIS.

In addition to the Raman signal, we also analyzed the elastic diffuse reflectance of the laser light, which was extracted from the same spectra as the Raman signals (Fig. 5). The elastic signal was much more sensitive to variations of μ_s' and less sensitive to μ_a. As a consequence, a simple ratio of Raman and elastic diffuse reflectance signal still depended on μ_a and μ_s' and therefore was not sufficient for correction in this

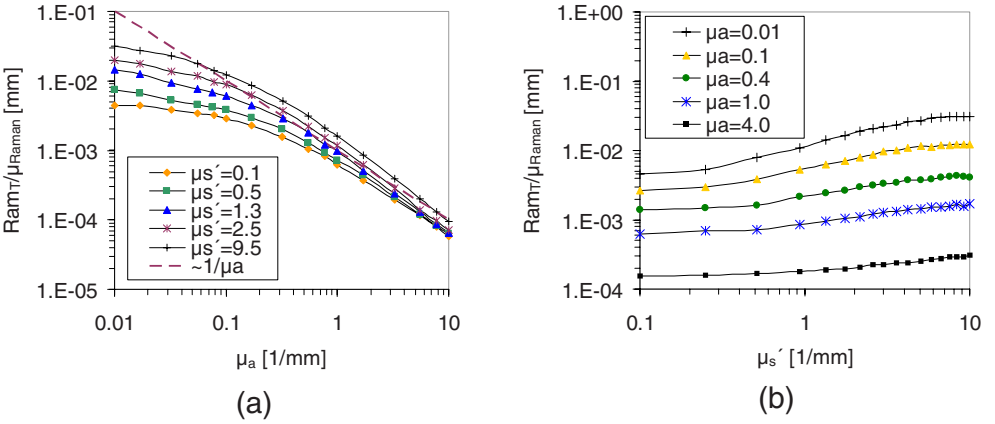

Fig. 4 Dependency of the simulated Raman signal Ram_T on the optical properties of the tissue matrix for our measurement geometry, where μ_a and μ_s' correspond to the mean of the optical properties at Raman and Stokes wavelength in units of 1/mm. (a) μ_a dependency: μ_s' is increasing from bottom to top. (b) μ_s' dependency: μ_a is increasing from top to bottom. Ram_T is defined as N_{Raman}/N_{ex} and is normalized by the unknown μ_{Raman}. In the VIS, Ram_T is roughly proportional to $1/\mu_a$. The influence of μ_s' is smaller but not neglible.

parameter range, which covered tissue optical properties in the VIS.

4 Determination of μ_{Raman} by Correction Functions

To link Raman signals from turbid samples directly to Raman scattering coefficients, we had to correct the Raman signal for the influence of the macroscopic optical properties. The measured or calculated relative Raman signal, which depended on μ_a, μ_s', and μ_{Raman} but also on the sample geometry, measurement geometry, and sensitivity of the setup, is called Ram_T. We assumed that the application of a dimensionless correction function $F(\mu_a, \mu_s')$, which was sample and measurement geometry-dependent, led to

$$Ram_T(\mu_a, \mu_s') \times F(\mu_a, \mu_s') = s \times l_0 \times \mu_{Raman}. \quad (1)$$

The right-hand side of Eq. (1) is independent from μ_a and μ_s' of the sample and can be interpreted as the signal that could be measured if the sample were transparent, similar to that defined in Refs. 12–14. The factor s, in units of Ram_T, depends only on the geometry and the sensitivity of the setup. The constant l_0 is the average pathlength of excitation photons in the transparent sample for the given sample and measurement geometry. In the case of a simulation (data not shown) where a transparent layer of Raman scatterers with refractive index $n=1$ was measured in backscattering geometry using an ideal detector (NA=1), $s \to \frac{1}{2}$ was obtained and l_0 corresponded to the layer thickness. The factor $s \times l_0$ can be obtained by measuring a calibration sample of the same geometry and known $F(\mu_a, \mu_s')$ and μ_{Raman}. For many applications, it might be sufficient to correct Ram_T relative to a reference sample of the same geometry with $\mu_{a,ref}$ and $\mu_{s,ref}'$ by

$$Ram_T(\mu_a, \mu_s') \times \frac{F(\mu_a, \mu_s')}{F(\mu_{a,ref}, \mu_{s,ref}')} = Ram_T(\mu_{a,ref}, \mu_{s,ref}'). \quad (2)$$

Next we will describe two types of the correction function F. Motivated by the existing literature, we investigated correction functions that utilize the elastic diffuse reflectance, which

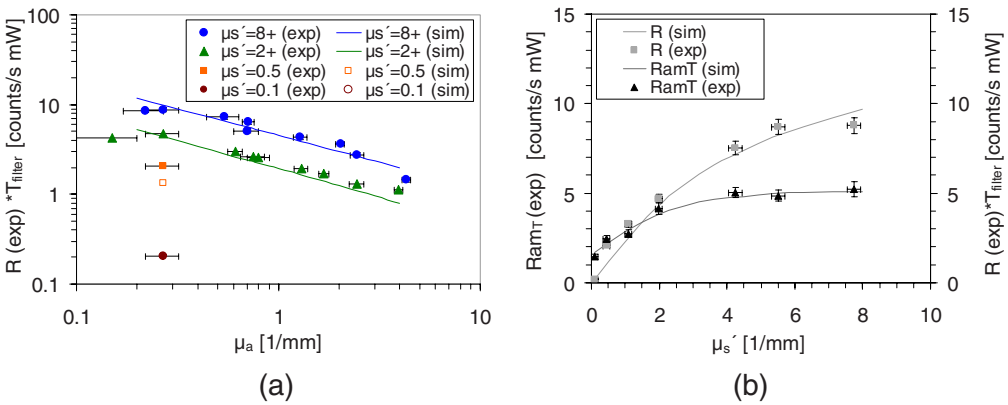

Fig. 5 (a) Comparison of experimental (filled symbols) and calculated results (lines, open symbols) for the dependency of the elastic diffuse reflectance signal (R) on μ_a for various series on μ_s', where μ_a and μ_s' correspond to the mean of the optical properties at the Raman and Stokes wavelength in units of 1/mm. The data for $\mu_s'=4$ mm^{-1} and $\mu_s'=6$ mm^{-1} are not included in the graph for clarity. (b) Comparison of experimental and simulated results (fitted to experiments) for the dependency of the Raman signal (Ram_T) and elastic diffuse reflectance signal (R) on μ_s' for $\mu_a=0.25$ mm^{-1}. The elastic scattering signal was attenuated by a long-pass filter ($\approx$OD6).

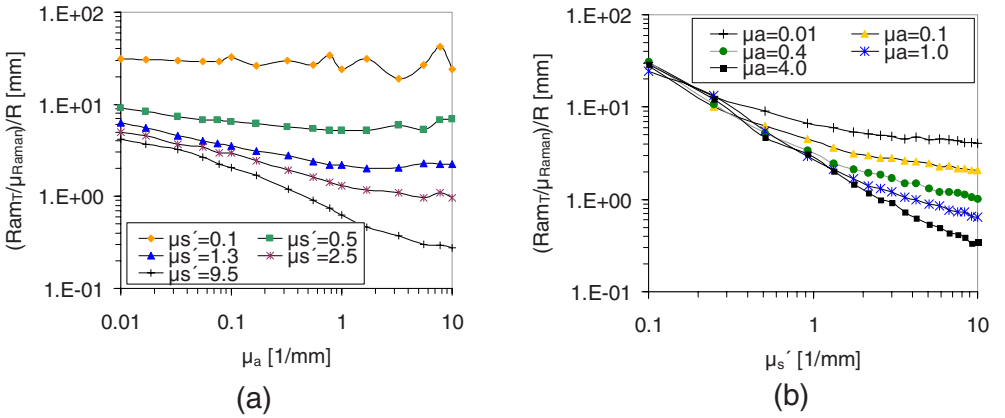

Fig. 6 Dependency of the ratio of simulated Ram_T to elastic diffuse reflectance R on the optical properties (given in units of 1/mm) for our measurement geometry. (a) μ_a dependency: μ_s' is increasing from bottom to top. (b) μ_s' dependency: μ_a is increasing from top to bottom.

is measured in the same geometry as the Raman signal (Sec. 4.1). We also suggest an alternative correction function that is based only on the simulations of the Raman signal (Sec. 4.2).

4.1 *Correction Utilizing the Elastic Diffuse Reflectance Signal*

It would be very convenient if a simple ratio of Ram_T and R could completely remove the influence of the optical properties. However, as shown for our measurement geometry in Fig. 6, the ratio only decreases the influence of μ_a. The influence of μ_s' increases except for the parameter range μ_a=0.01 to 0.1 mm^{-1} and $\mu_s' > 0.4$mm^{-1}, where the influence of μ_s' decreases as well. This explains why the ratio improved the results in Ref. 14, where a measurement spot of similar size was used ($r_{ex} \approx r_{det} \approx 1$ mm).

In Fig. 7(a), Ram_T is plotted versus R for various combinations of μ_a and μ_s' and for three different measurement geometries. Obviously, Ram_T cannot be described as a function of R only without knowledge of the other variables. However, it was shown recently for measurements in the NIR that $Ram_T \times \mu_t$, with $\mu_t = \mu_a + \mu_s$, can be described by a function of R only; see Refs. 12 and 13. This leads to the correction function $F_1 = \mu_t \times l_1 / f_1(R)$, where $f_1(R)$ is a geometry-dependent function of the diffuse reflectance (R), and l_1 is a length to make F dimensionless as defined in Eq. (1). Using our Monte Carlo model, we searched for similar empirical correction functions and evaluated their validity with respect to the range of optical properties and the measurement geometry. While we found some correction functions that were only valid in the semi-infinite measurement geometry or the VIS parameter range, only F_1 and $F_2 = \mu_s' \times l_2 / f_2(R)$ could be used for our measurement geometry in the whole parameter range investigated here. Since F_1 and F_2 performed very similarly, we present only the application of F_2 in Fig. 7(b). It is obvious that F_2 works in the semi-infinite as well as in our measurement geometry, but not for a measurement spot with a diameter of 200 μm. In order to find a function $f_2(R)$ for the whole parameter range, we applied a 4th-order polynomial to

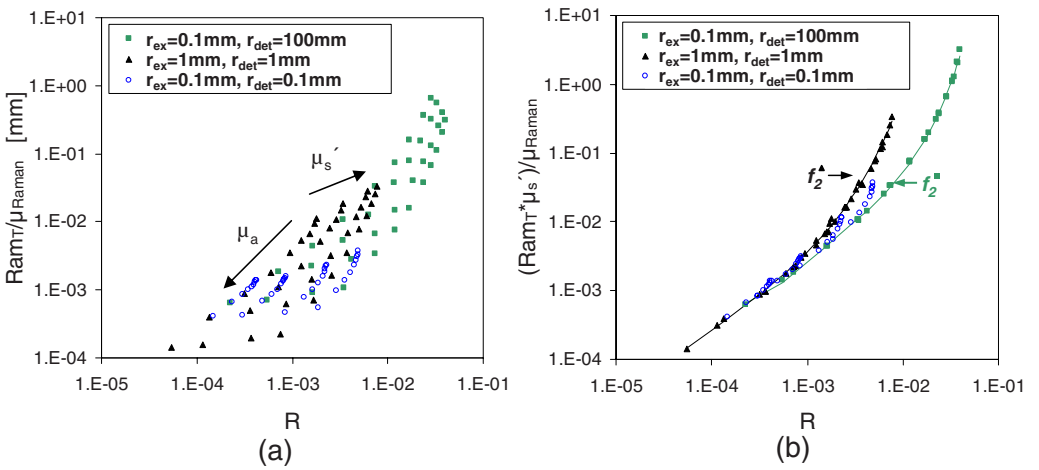

Fig. 7 (a) Ram_T cannot be described as a function of R only without knowledge of the optical properties and the geometry. (b) $Ram_T/\mu_{Raman} \times \mu_s'$ can be described as a geometry-dependent function of R only, but not for all possible measurement geometries. The optical properties used to calculated the data points are μ_a=[0.01, 0.02, 0.05, 0.1, 0.2, 0.5, 1, 5 mm^{-1}] from top to bottom, and μ_s'=[1,2,5,10 mm^{-1}] from left to right. The different symbols correspond to three different measurement geometries in terms of the radius of excitation r_{ex} and detection fiber r_{det}: (1) r_{ex}=0.1 mm, r_{det}=100 mm; (2) r_{ex}=1.5 mm, r_{det}=0.7 mm; (3) r_{ex}=0.1 mm, r_{det}=0.1 mm.

the log of the data. We accounted for different optical properties at the excitation and Stokes wavelength by using the mean optical properties. A wavelength-dependent variation of R can be accounted for by using the geometric mean $\sqrt{R_{ex}R_s}$ instead.

When F_2 was applied to the simulated data in Fig. 4, the variation of the data decreased from 109% to 6%. This means that the accuracy of the μ_{Raman} to be determined is strongly improved. When F_2 was applied to our silicone phantom data (Sec. 2.3), the variation of the data decreased from 88% to 21%. The remaining variability of the signal could result from variations in the sample preparation and from the fact that the diffuse reflectance was only measured at the excitation wavelength. Therefore, an experimental investigation of the correction effect was limited with this setup.

4.2 *Correction Based on Raman Signal Simulations*

Since our Monte Carlo model for Raman measurements in turbid media corresponded sufficiently well with our experiments, we also used directly the forward simulation of $Ram_T(\mu_a,\mu_s')/\mu_{Raman}$ to obtain the correction function F_{MC} according to Eq. (1). For a relative correction according to Eq. (2), we simulated

$$F(\mu_a,\mu_s')/F(\mu_{a,ref},\mu_{s,ref}') = Ram_T(\mu_{a,ref},\mu_{s,ref}')/Ram_T(\mu_a,\mu_s').$$

To minimize the computational effort during the measurement, the correction factors were simulated once for various combinations of μ_a and μ_s' and stored in a table. To account for the different optical properties at the excitation and Stokes wavelength, $Ram_T(\mu_a,\mu_s')$ can be replaced by the geometric mean of $Ram_T(\mu_a,\mu_s')$ at both wavelengths. However, if the values are simulated *a priori*, using four variables would drastically increase the size of this table. Therefore, it is more convenient to use the Raman signal at the mean optical properties of excitation and Stokes wavelength, which we found to be equal to the letter approach in the case of $\mu_a \leqslant \mu_s'$.

The effect of this correction procedure on the simulated data led to a straight line (not shown). When applied to the phantom data, the variation of the data decreased from 88% to 16%. The remaining variability of the signal could be due to variations in the sample preparation.

5 Determination of Molecular Raman Cross Section or Raman Scatterer Concentration

In Sec. 4 we described how μ_{Raman} could be determined once the calibration factors were measured. Another way to determine μ_{Raman} independent from a calibration measurement is by comparing the simulated ratio of the Raman to elastic signal (see Fig. 6) to the measured ratio given in Fig. 5(b). We estimated the magnitude of μ_{Raman} to be $\approx 3\times10^{-7}$ mm^{-1} for our phantoms with 10 μg/ml ($\approx 2\times10^{-5}$ M).

For known Raman scatterer concentration c and μ_{Raman}, the differential molecular Raman scattering cross-section σ can be calculated by

$$\sigma = \frac{\mu_{Raman}}{4\pi \times c}. \quad (3)$$

We obtained $\sigma = 2\times10^{-23}$ cm^2 molecule^{-1} Sr^{-1} for our silicone phantoms. Compared to the results of Berdyugin et al.[21] (3.2×10^{-24} cm^2 molecule^{-1} Sr^{-1}, measured in cyclohexane at 514 nm excitation and concentration of 2×10^{-6} M), our result was one order of magnitude larger. This can be at least partially explained by the enhanced resonance excitation at 488 nm. Surprisingly, the results of Tian et al.[22] varied up to 3 orders of magnitude (10^{-24} to 10^{-21} cm^2 molecule^{-1} Sr^{-1}) depending on the β-carotene concentration (10^{-6} to 10^{-10} M), which was dissolved with pyridine and diluted with water. Thus, for the absolute quantification of β-carotene in biomedical applications, more investigations of the molecular resonance Raman cross-section in different biological matrices and for different concentrations should be performed.

Assuming the molecular Raman scattering cross-section σ can be found in the literature, the concentration c of the Raman scatterer can be calculated by Eq. (3) using the measured μ_{Raman}.

6 Summary and Discussion

We introduced a method to combine Raman and spatially resolved reflectance spectroscopy that allows the measurement of the optical properties together with the Raman spectrum. To determine the absolute Raman scatterer coefficients μ_{Raman} independent from the optical properties, we compared to different methods to correct for the turbidity-induced signal variation. One correction method utilized empirical functions that are dependent on the elastic diffuse reflectance but also require knowledge of the optical properties. An alternative method used a Monte Carlo model to generate and propagate Raman signals in turbid media to directly calculate the correction factors, regardless of any functional relationship.

Both correction methods reduced the turbidity-induced signal variation by 95% or more for our simulated data, and by 76% or more for our phantom data. Both correction methods need to be adjusted once to the excitation and the detection using phantom measurements or Monte Carlo simulations. Since the empirical equations still require knowledge of the optical properties, we see no advantage to this method. The correction method based on the Monte Carlo simulation, however, does not require the measurement of elastic reflectance in the Raman measurement geometry and can even be used in geometries such as a 200-μm measurement spot, where an empirical correction function has not been described yet. For the data presented here, we used correction functions obtained for samples that were homogenous within the sampling volume. However, this simplification may be critical if a sampling volume includes different layers, like the epidermis and the dermis in skin measurements. The influence of the sample structure on the correction function is the subject of a current investigation.

From the determined μ_{Raman}, we calculated the molecular Raman scattering cross-section σ of a given β-carotene concentration in our silicone phantoms. For a known σ, the absolute Raman scatterer concentration can be determined from μ_{Raman}. For unknown molecular Raman cross-sections, which

is a possible scenario especially in complex biological matrices, the methods can also correct Raman signal variations induced by sample-to-sample turbidity variation, which allows the quantitative comparison of results obtained from different individuals, tissues, or tissue sites.

Although we took advantage of the outstanding high-resonance Raman scattering cross-section of β-carotene, the correction methods are transferable to any other Raman scatterer. For the correction of multiple Raman peaks at different wavelengths, the optical property measurement can be easily performed using white light instead of lasers. In addition to biomedical applications, the correction method might also be beneficial in the food industry or environmental research, where quantitative measurements of analytes independent of turbidity variations are necessary. Furthermore, we suggest that the correction procedures may be applied similarly to fluorescence measurements.

Acknowledgments

We thank M. Meinke and M. Darvin (Center of Experimental and Applied Cutaneous Physiology, Charité-Universitätsmedizin Berlin) for useful discussions. The project was funded by the Senate of Berlin and by the European Union (EFRE, FKZ 10138595).

References

1. A. S. Haka, K. E. Shafer-Peltier, M. Fitzmaurice, J. Crowe, R. R. Dasari, and M. S. Feld, "Diagnosing breast cancer by using Raman spectroscopy," *Proc. Natl. Acad. Sci. U.S.A.* **102**(35), 12371–12376 (2005).
2. M. D. Keller, E. M. Kanter, C. A. Lieber, S. K. Majumder, J. Hutchings, D. L. Ellis, R. B. Beaven, N. Stone, and A. Mahadevan-Jansen, "Detecting temporal and spatial effects of epithelial cancers with Raman spectroscopy," *Dis. Markers* **25**, 323–337 (2008).
3. A. Nijssen, S. Koljenovic, T. C. Bakker Schut, P. J. Caspers, and G. J. Puppels, "Towards oncological application of Raman spectroscopy," *J. Biophotonics* **2**, 29–36 (2009).
4. S. W. E. van de Poll, K. Kastelijn, T. C. Bakker Schut, C. Strijder, G. Pasterkamp, G. J. Puppels, and A. van der Laarse, "On-line detection of cholesterol and calcification by catheter based Raman spectroscopy in human atherosclerotic plaque *ex vivo*," *Heart* **89**(9), 1078–1082 (2003).
5. A. J. Berger, T. W. Koo, I. Itzkan, G. Horowitz, and M. S. Feld, "Multicomponent blood analysis by near-infrared Raman spectroscopy," *Appl. Opt.* **38**, 2916–2926 (1999).
6. D. Arifler, C. MacAulay, M. Follen, and R. Richards-Kortum, "Spatially resolved reflectance spectroscopy for diagnosis of cervical precancer: Monte Carlo modeling and comparison to clinical measurements," *J. Biomed. Opt.* **11**(6), 064027 (2006).
7. E. Salomatina, B. Jiang, J. Novak, and A. N. Yaroslavsky, "Optical properties of normal and cancerous human skin in the visible and near-infrared spectral range," *J. Biomed. Opt.* **11**, 064026 (2006).
8. R. Reif, O. A'Amar, and I. J. Bigio, "Analytical model of light reflectance for extraction of the optical properties in small volumes of turbid media," *Appl. Opt.* **46**(29), 7317–7328 (2007).
9. M. Pilz, S. Honold, and A. Kienle, "Determination of the optical properties of turbid media by measurements of the spatially resolved reflectance considering the point-spread function of the camera system," *J. Biomed. Opt.* **13**(5), 054047 (2008).
10. S. J. Tinnemans, M. H. F. Kox, T. A. Nijhuis, T. Visser, and B. M. Weckhuysen, "Real time quantitative Raman spectroscopy of supported metal oxide catalysts without the need of an internal standard," *Phys. Chem. Chem. Phys.* **7**, 211–216 (2005).
11. D. N. Waters, "Raman spectroscopy of powders—Effects of light absorption and scattering," *Spectrochim. Acta Mol. Spectros.* **50**, 1833–1840 (1994).
12. W. C. Shih, K. L. Bechtel, and M. S. Feld, "Intrinsic Raman spectroscopy for quantitative biological spectroscopy Part 1: Theory and simulations," *Opt. Express* **16**(17), 12726–12736 (2008).
13. K. L. Bechtel, W. C. Shih, and M. S. Feld, "Intrinsic Raman spectroscopy for quantitative biological spectroscopy Part 2: Experimental applications," *Opt. Express* **16**(17), 12737–12745 (2008).
14. I. Barman, G. P. Singh, R. R. Dasari, and M. S. Feld, "Turbidity-corrected Raman spectroscopy for blood analyte detection," *Anal. Chem.* **81**, 4233–4240 (2009).
15. G. Zonios and A. Dimou, "Light scattering spectroscopy of human skin *in vivo*," *Opt. Express* **17**(3), 1256–1267 (2009).
16. C. Reble, I. Gersonde, S. Andree, J. Helfmann, and G. Illing, "Correction of Raman signals for tissue optical properties," *Proc. SPIE* **7368**, 73680C (2009).
17. L. H. Wang, S. L. Jacques, and L. Q. Zheng, "MCML Monte Carlo modeling of photon transport in multi-layered tissues," *Comput. Methods Programs Biomed.* **47**, 131–146 (1995).
18. N. Rajaram, T. H. Nguyen, and J. W. Tunnell, "Lookup table-based inverse model for determining optical properties of turbid media," *J. Biomed. Opt.* **13**(5), 050501 (2008).
19. S. Andree, C. Reble, J. Helfmann, I. Gersonde, and G. Illing, "Spatially resolved reflectance to deduce absorption and reduced scattering coefficients," *Proc. SPIE* **7368**, 73680I (2009).
20. M. Friebel, A. Roggan, G. Müller, and M. Meinke, "Determination of optical properties of human blood in the spectral range 250 to 1100 nm using Monte Carlo simulations with hematocrit-dependent effective scattering phase functions," *J. Biomed. Opt.* **11**(3), 034021 (2006).
21. V. V. Berdyugin, K. Y. Burshtein, and P. P. Shorygin, "Cross section of resonance Raman scattering of light by polyenes," *Opt. Spectrosc.* **61**(2), 192–194 (1986).
22. Y.-J. Tian, J. Zuo, L.-Y. Zhang, Z.-W. Li, S.-Q. Gao, and G.-H. Lu., "Study of resonance Raman cross section of aqueous β-carotene at low concentrations," *Appl. Phys. B* **87**(4), 727–730 (2007).